



Analysis of exergy in a dimple-roughened solar thermal collector using MATLAB simulation

Raj Kumar^{1,7} · Muneesh Sethi² · Abhishek Thakur³ · Adit Rana⁴ · Varun Goel⁵ · Daeho Lee¹ · Tej Singh⁶

Received: 20 April 2024 / Accepted: 5 October 2024 / Published online: 16 December 2024
© The Author(s) 2024

Abstract

In the current study, the performance of a dimple-roughened solar thermal collector (DRSTC) is investigated within a (Re_{xx}) range that spans from 3000 to 48,000. Under constant solar intensity ($I_{sr}=1000 \text{ Wm}^{-2}$), relative roughness height (e_d/D_h) varied from 0.021 to 0.036, relative roughness pitch (p/e_d) from 10 to 20, arc angle (α_a) from 45 to 60°, and temperature rise parameter from 0.003 to 0.02, and the proposed model predicts exergy efficiency of the SAH, and the results obtained can be used as reference for the design of new solar thermal systems. The assessment makes use of advanced MATLAB simulations in order to evaluate the exergetic efficiency (η_{ex}) of a DRSTC. At lower Re_{xx} values, (η_{ex}) increases uniformly; however, stabilization and decline occur at higher Re_{xx} values. The highest (η_{ex}) for the DRSTC is 1.47% under a temperature rise parameter ($\Delta T/I_{sr}$) of 0.0071 Km^2W^{-1} for obtaining optimum values of $e_d/D_h = 0.036$, $p/e_d = 10$, and $\alpha_a = 60^\circ$. This research illustrates the usefulness of MATLAB for solar energy system analysis and optimization by integrating simulation and experimental data. This investigation further supports the feasibility of the proposed collector design.

Keywords Renewable energy · Solar energy · Solar thermal collector · Absorber plate with dimple roughness · Nusselt number · Exergetic efficiency

List of symbols

A_p	Plate (absorber) surface area, m^2
C_{pa}	Specific heat of air, $\text{Jkg}^{-1}\text{K}^{-1}$
W_{ap}	Width of absorber plate

D_h	Hydraulic diameter, m
$(\Delta P)_d$	Pressure drop across test section, Pa
Nu_{ss}	Nusselt number for smooth surface
H_d	Duct height, m
L_t	Test section length of duct, m
h_w	Convective heat transfer coefficient due to wind, $\text{Wm}^{-2}\text{K}^{-1}$
L_g	Air gap between absorber plate and glass cover, m
N	Number of glass cover
P_{atm}	Atmospheric pressure, Pa
U_1	Overall heat loss co-efficient, $\text{Wm}^{-2}\text{K}^{-1}$
t_g	Thickness of cover (glass), m
T_{amb}	Ambient temperature, K
t_i	Thickness of thermal insulation, m
T_o	Air outlet temperature, K
U_b	Bottom heat loss coefficient
k_{air}	Thermal conductivity of air $\text{Wm}^{-1}\text{K}^{-1}$

Raj Kumar and Muneesh are Joint first author.

✉ Daeho Lee
dhl@gachon.ac.kr

✉ Tej Singh
sht@inf.elte.hu

¹ Department of Mechanical Engineering, Gachon University, Seongnam 13120, South Korea

² COER University, Roorkee, Uttarakhand 247667, India

³ School of Physics & Materials Science, Shoolini University, Solan, Himachal Pradesh 173229, India

⁴ Department of Mechanical Engineering, Sri Sai University, Palampur, Himachal Pradesh 176081, India

⁵ Department of Mechanical Engineering, National Institute of Technology, Hamirpur, Himachal Pradesh 177005, India

⁶ Faculty of Informatics, Savaria Institute of Technology, ELTE Eötvös Loránd University, Budapest 1117, Hungary

⁷ Jindal School of Environment & Sustainability, O.P. Jindal Global University, Sonapat 131001, Haryana, India

V_a	Mean flow velocity in duct, ms^{-1}	ΔT	Temperature rise in air, K
V_w	Wind velocity, ms^{-1}	ε_g	Emissivity of the glass cover
W_d	Width of duct, m	ε_p	Emissivity of the absorber plate
SAH	Solar air heater	η_{ex}	Exergetic efficiency
STC	Solar thermal collector	η_f	Fan efficiency
SC	Solar collector	SWH	Solar water heater
μ_a	Dynamic viscosity, Ns m^{-2}	η_m	Electric motor efficiency
ρ_a	Density, Kg m^{-3}	η_{th}	Thermal efficiency
$\tau\alpha$	Transmittance-absorptance product	η_{tr}	Transmission efficiency
E_{nf}	Exergy flow to fluid, W	T_p	Mean temperature of absorber plate, K
η_c	Carnot efficiency	m_{air}	Mass flow rate of air, kg s^{-1}
e_d/D_h or R_h	Relative roughness height	p/e_d or R_p	Relative roughness pitch
$\dot{Q}_u, \dot{Q}_{u1}, \dot{Q}_{u2}$	Useful heat gain, W	$\Delta T/I_{\text{sr}}$ or $[(T_o - T_i)/I_{\text{sr}}]$	Temperature rise parameter, Km^2W^{-1}
η_{thp}	Thermo-hydraulic performance parameter	E_{sr}	Exergy flow associated with solar irradiance, W
β_{ta}	Tilt angle, $^\circ$	α_a	Arc angle, $^\circ$
F	Plate efficiency or collector efficiency factor	h_t	Convective heat transfer coefficient, $\text{Wm}^{-2}\text{K}^{-1}$
η_{eff}	Effective efficiency	η_{en}	Energy efficiency
MADM	Multi-attribute decision-making approach	DRSTC	Dimple-roughened solar thermal collector
CFD	Computational fluid dynamics	DP	Double pass
AP	Absorber plate	STS	Solar thermal system
HT	Heat transfer	Solar Energy	SE
e_d	Depth of dimple, m		
d	Dimple print diameter, m		
L_{ap}	Length of absorber plate		
f_{xx}	Friction factor		
G_a	Mass velocity of air, ms^{-1}		
f_{ss}	Friction factor for smooth surface		
I_{sr}	Intensity of solar radiation, Wm^{-2}		
U_t	Heat-loss coefficient (top), $\text{Wm}^{-2}\text{K}^{-1}$		
k_i	Thermal conductivity of insulation, $\text{Wm}^{-1}\text{K}^{-1}$		
F_r	Heat removal factor based on outlet air temperature		
Nu_{xx}	Nusselt number		
p	Pitch, m		
T_s	Equivalent temperature of the Sun as a blackbody		
Re_{xx}	Reynolds number		
T_i	Inlet temperature, K		
t_e	Thickness of edge (collector), m		
T_f	Mean bulk fluid temperature, K		
P_m	Mechanical power		
U_e	Heat-loss coefficient (edge), $\text{Wm}^{-2}\text{K}^{-1}$		

Introduction

Globally, the requirement for energy is rising quickly to suit the demands of both industrial and residential consumers. To fulfill this energy need, almost 80% of the world's main energy comes from fossil fuels. But the primary issue facing fossil fuels is the growing demand and quick depletion of these resources. However, using fossil fuels has detrimental effects on the environment and human health. Because of these environmental and health issues, researchers have been focusing on clean and renewable energy sources in recent years [1–4]. Consequently, clean and renewable energy has become more and more popular in recent times [5–7]. Worldwide, SE is frequently used since it is an endless, clean, and renewable energy source [8–11]. Sunlight is a source of both thermal and electrical energy. Thermal energy attained from solar radiation is extensively used in many applications, including air conditioning, refrigeration, drying, heating of space, greenhouses, and preheating [12–15]. Solar thermal applications have an inexpensive, straightforward design. SWH and SAH are two important types of STCs, being used prominently. Hot water for industrial or construction purposes may be affordably provided by SWHs [16–18]. SAH has a restricted range of uses, but its efficiency in thermal applications is around three times

higher than its efficiency in solar power generating applications [19–22]. Since SAHs have a narrow temperature range, they are recommended for applications that need low temperatures. To augment the SCs efficiency, several scientists have experimented with various methods. These techniques include twisted tape, baffles, slotted and filled absorbers, and fin design. The aim of all these techniques is to increase the heat transmission from the AP to the surrounding air [23–25]. Chauhan et al. [26] evaluated the features of the η_{eff} distribution in an STC channel with protruding and dimpled arc turbulators in the air stream path. Alrashidi et al. [27] assessed the correct SAH's tilt angle by analyzing its η_{en} and η_{ex} using data from summer tests. According to the findings of the energy analysis, tilting SAH at $\theta = 20^\circ$ produces an extreme η_{ex} of 26.4% at midday, a sustainability index of 1.36, and a 46 W potential enhancement. Sharma et al. [28] analyzed the solidification and melting characteristics of numerous shell and tube type latent heat storage unit (ST-LHSU) designs that might be used STS at low-temperature. For the research, four different ST-LHSU designs were taken into consideration and examined by use of a numerical model in 2-dimensional. Arunkumar et al. [29] demonstrated a unique way to create a double-chamber system for SAHs by adding many inlets to the absorber portion. Geometric characteristics that are parametrically modified include the diameter of the hole on the AP and the cross section of the input duct. Chauhan et al. [30] evaluated the dimpled/protruded absorbers in STC about their thermo-hydraulic performance. In addition, a measure of both benefits and disadvantages are assessed using the VIKOR approach, and lastly, the VIKOR index is used to rank the options that are arranged from best to worst. Nu_{xx} for protruded and dimpled arcs have been found to be 2.24 and 3.65 times, respectively, whereas the corresponding f_{xx} enhancements are 2.65 and 1.6 times. Additionally, it is noted that for dimpled-arc and protruded-arc absorbers, there is an increase of 1.22 and 1.23 times for η_{eff} and 1.36 and 1.09 times for η_{ex} compared to conventional collectors. Kushwaha et al. [31] investigated the desiccant wheel-based solar powered atmospheric water harvesting system's performance both theoretically and experimentally. Utilizing the energy and exergy aspects, the system's performance has been assessed. With an energy efficiency of 2.56%, the system may attain an average exergy efficiency of 9.83%. Chamoli et al. [32] examined the heat transmission and friction loss properties in a horizontal rectangular channel with circular profile fin attachments across one of its heated sides using CFD. It was discovered that the stream-wise pitch of 3 at 5000 Re_{xx} has an overall enhancement ratio that reaches a maximum value of 1.2. Bhattacharyya et al. [33] carried out research using an experiment to investigate the properties of pressure drop and heat transmission in a circular heat exchanger tube with staggered angular cut baffle and inline angular cut baffle. A range of Re_{xx} , from

10,000 to 52,000, as well as various baffle pitch ratios and cutting angles, have all been tested in these experiments. The current baffle layouts function better than existing turbulators, based on the findings. Sharma et al. [34] explored the solidification capabilities of an LHSU of the concentric tube type with various herringbone-patterned, wavy fin models. A commercially available CFD solver has been used to construct a validated 2-dimensional transient solidification HT model for an LHSU with several herringbone wavy fin shapes. Fattoum et al. [35] described an experimental study of the double flow SAH using wire mesh packing in the upper and lower ducts of different lengths, and important conclusions are offered. When compared to the standard SAH design, the modified SAH design displayed outstanding performance in terms of the temperature differential and the energy efficiency. Pachori et al. [36] evaluated the thermohydraulic performance parameter (THPP) of a SAH integrated with V-shaped ribs using a mix of analytical and CFD approaches. Specifically, exergy and thermal efficiency were taken into consideration when comparing the findings of the investigation to that of a smooth SAH. Sethi et al. [37] explored the consequence of artificial roughness on Nu_{xx} and friction factor characteristics in a SAH channel with dimple-shaped elements organized in an arc pattern on the AP. Experimental research was done on a range of systems and operational settings. Using the experimental data, correlations between the Nu_{xx} and f_{xx} have been constructed as functions of roughness characteristics and operational parameters.

The exergy analysis can further be carried out for SAH for different varieties of roughness geometries to minimize the exergy losses. Kumar et al. [38] used the 2nd law of thermodynamics as a framework to investigate the performance of a spherical dimpled SAH in a turbulent environment. This study considers the component-wise exergy potential losses, the overall exergy efficiency, and their differentials. Bhuvad et al. [39] investigated SAH with apex up-flow discrete-arc-rib roughened geometry for η_{th} and η_{ex} . The α_a was varied from 30° to 60° , and the values of parameters gap width (g/e_d), e_d/D_h and p/e_d were fixed at 4, 0.045 and 10, respectively. The results were compared with recently developed SAH. The highest η_{th} and η_{ex} were reported as 82.2% and 4.14%, at $\Delta T/I_{\text{sr}} = 0.0377 \text{ Km}^2\text{W}^{-1}$. The optimum values of roughness geometries obtained are $\alpha_a = 30^\circ$, $g/e_d = 4$ and $p/e_d = 10$. It was also observed that loss in optical exergy does not depend upon the Re_{xx} and roughness geometry in the form of ribs result in the rise of pumping power; however, the increment is quite low and does not impact the net energy gain. Nidhul et al. [40] analyzed energy and exergy efficiency for W-Baffles and semi-cylindrical walled SAH and performed CFD analysis to predict the behavior of SAH. The analysis was performed with Re_{xx} values from 5000 to 17500; however, baffle inclination (β), R_h and R_p were varied for optimum conditions. The turbulence was increased

by molding the corners, and effectiveness was enhanced by 127% in comparison with smooth SAH. Correlations were generated based upon CFD analysis, and an enhancement of 40.7% and 95.4% was obtained for η_{th} and η_{ex} in comparison with conventional SAH. Luan et al. [41] developed correlation in terms of Nu_{xx} and f_{xx} for a SAH with inclined baffles, based upon experimental data and performed exergy analysis. A baffle angle from 60 to 120°, $Re_{xx} = 24,000$ resulted in maximum efficiency of 63%, and the η_{ex} was observed to be with maximum value of 0.7% at Re_{xx} of 1500. Thapa et al. [42] analytically investigated η_{th} and η_{ex} of parabolic trough receiver using simulation software. The rise in m_{air} increases the exergy loss, having an increasing slope with rising $\Delta T/I_{sr}$. The optimal values of twist ratio, perforation ratio and winglet ratio were found to be 3, 0.05 and 0.1, respectively, corresponding to maximum η_{ex} . Harikrishnan et al. [43] conducted indoor experimentation on a downward solar air heater (DSAH) with and without impingement of jets and η_{ex} was calculated along with exergy losses. The consequence of numerous stream parameters on η_{th} , η_{eff} and η_{ex} was evaluated. The maximum value of η_{eff} was 84.86% with optimum values of parameters: jet spacing = 0.5, $D_j/D_h = 0.057$ and $m_{air} = 0.06 \text{ kg s}^{-1}$. The η_{eff} and η_{ex} of DSAH with impinging jet have been observed to be within a range of 57.28–84.86% and 4.35–0.45%, respectively, when m_{air} is varied within a range of 0.02–0.06 kg s^{-1} with I_{sr} of 1000 W m^{-2} . Mortazavi et al. [44] performed advance exergetic analysis on smooth plate collector and collector with thin metal plate. Various mathematical models were developed with the help of energy balance equations of each component and thermodynamic processes were altered, and advanced exergy analysis was executed to comply with problem. The exergy analysis was performed using the Re_{xx} , channel depth and I_{sr} on the exergy destruction of each part. The results indicated that exergy destruction can be minimized in glass cover, whereas AP always results in large amount of energy destruction and is unavoidable. Nidhul et al. [45] conducted CFD study of SAH having triangular duct with V-rib roughness geometry, and results were compared with other roughness geometries inscribed on triangular and rectangular ducts. The enhancement in Nusselt number is 2.53 times the smooth collector for $e_d/D_h = 0.05$, $p/e_d = 10$, and $\alpha_a = 45^\circ$ at $Re_{xx} = 7500$, whereas the rise in f_{xx} is observed to be 2.53 times in comparison with smooth plate. Effectiveness parameter has maximum value equal to 2.01 for $\alpha_a = 45^\circ$ at $Re_{xx} = 7500$. Based upon the correlations developed using CFD analysis, Nu_{xx} and f_{xx} were predicted, η_{ex} was computed and maximum enhancement of 23% was obtained. It was deduced that V ribbed triangular duct SAH at $\alpha_a = 45^\circ$ can be used in heat exchangers requiring compact design as compared to a ribbed rectangular duct SAH. Hassan et al. [46] examined noble tubular SAH (VTSAH) and correlated its performance with ordinary tubular SAH (OTSAH) for single pass (SP) and double pass (DP) stream conditions with varying m_{air} . There is significant rise in outlet temperature of air, energy and exergetic performance and

thermodynamic efficiency as compared to OTSAH. DP gives higher value of T_o , η_{th} , η_{eff} and η_{ex} , as compared to SP solar air heater. At m_{air} of 0.072 kg s^{-1} for DP, the η_{th} of VTSAH is observed to be 88.4%; however, OTSAH and flat plate SAH efficiency have been found to be 77.3%, and 72%, respectively. The calculated value of exergy efficiency of 3.89% is obtained for VTSAH. Kumar et al. [47] experimentally investigated V-corrugated geometry on AP and modified it with the help of shot blasting. It is inferred that SAH is useful in reducing moisture from agriculture products. It was observed that for m_{air} of 0.01, 0.015, and 0.02 kg s^{-1} in SAH, the η_{th} and η_{ex} enhanced by 2.4%, 3.1%, 5.8% and 0.21, 0.36, 0.70, respectively, as compared to smooth collector. The economic factors pertaining to environment were also augmented by 23.4%, 15.1%, and 18.2% on the prescribed flow rates, and the system diminishes the CO_2 by 10.3–28.7 tons per year. It was further observed that new designs of SAH can be developed with shot blasting technique for drying of agriculture products. Abdelkader et al. [48] experimentally investigated SAH having selective novel coating of carbon nanotubes (CNT) and CuO nanoparticles embedded into black paint on AP. There is a rise in the absorptivity of the AP, resulting in rise in HT and a notable enhancement in η_{en} and η_{ex} . The investigation resulted in high value of exergy efficiency with new selective coating. It was suggested that SAH with black coatings can relate to heat storage medium and solar drying unit for further investigation. Khanlari et al. [49] numerically and experimentally analyze the consequence of incorporating a nano-enhanced absorber coating to a vertical solar air heating system without glazing to improve its energetic and exergetic performance. In the initial phase of the study, computational fluid dynamics was used to explore numerous vertical SAH designs, such as hollow, baffled, and perforated baffled systems. Numerical findings indicated that the system with perforated baffles (PBs) offered the most effective performance indicators. Two heating systems involving PBs have been constructed in this contest. Regular matt black paint was put on one of the systems, while black paint with CuO nano-embedded black paint was used for the other SAH. Hedge et al. [50] numerically investigated η_{eff} and η_{ex} of SAH with perforated holes on AP which are arranged in different rows. The highest η_{eff} (86.51% and 85.15%) was observed for rows of perforated holes having diameter ratio of hole = 0.06 and 0.07, respectively, corresponding to Re_{xx} value of 21,000. The maximum η_{ex} is 5.28% and the CO_2 mitigation rate is 1.12 tons per annum, based on environmental economic analysis. The calculated payback period of energy and exergy is 5 months and 22 years, respectively. Ghiami et al. [51] performed comparative analysis of novel SAH (with baffles and without baffles) with paraffin wax as PCM. Galvanized iron is used to fabricate baffles which were arranged on AP in sequential manner. Based upon 1st and 2nd law of thermodynamics, η_{th} and η_{ex} were evaluated for AP equipped with baffles and without baffles, and m_{air} was fixed at 0.017, 0.014 and 0.009 kg s^{-1} , respectively. SAH with baffles arranged in sequential order

yielded maximum exergy efficiency of 20.47% for $m_{\text{air}} = 0.017 \text{ kg s}^{-1}$. Avargani et al. [52] did CFD analysis to simulate the influence of obstacles on AP of SAH. The mathematical models were prepared, and the results obtained were collated with experimental values, while using obstacles of geometries like cylindrical, spherical, hemispherical, pyramidal, and cubical. It was observed that vertical cylindrical obstacles result in significant rise in η_{th} , η_{eff} , and η_{ex} when compared with various geometries. Sharma et al. [53] provided a thorough analysis of several collector-storage type solar water heating systems (SWHS) with latent heat storage (LHS), both integrated and standalone. The use of LHS considerably improves the thermal efficiency and efficacy of SWHS. In an effort to improve performance, Saleh Abo-Elfadl et al. [54] examined a V-shaped transverse finned SAH with lateral spaces and central openings. In comparison with the longitudinal finned heater, the SAH attains an uppermost exit temperature increase of 28.2 °C at 0.025 kg s⁻¹ and DP flow, with average daily η_{th} of 61.3%, 81.88%, and 88.5% at m_{air} of 0.025 kg s⁻¹, 0.05, and 0.075, representing increases of 9.66%, 13.3%, and 9.4%, respectively. Additionally, it attains greater η_{ex} of 1.7%, 2.1%, and 2.5% in comparison with the longitudinal finned heater at m_{air} of 0.075, 0.05, and 0.025 kg s⁻¹, representing increases of 18.2%, 25.7%, and 18%, respectively. Singh and Vardhan [55] examine the energy and exergy characteristics of helical coils that have been modified for use in a SAH. The improved SAH greatly enhances the η_{th} and the η_{ex} , achieving the greatest η_{ex} of 5.61%. The research conducted by Saleh Abo-Elfadl et al. [56] examines the efficiency of a DP SAH with pin-finned absorber under various air mass ratios. The pin-finned SAH has superior performance compared to the flat SAH in terms of air temperature increase, η_{th} and η_{ex} . The pin-finned SAH has a much better average η_{ex} of 34.7%. Reddy et al. [57] conducted an experiment where they fabricated a plastic SAH and examined its η_{th} and η_{ex} both with and without a polyethylene cover (0.5 mm thick). The analysis revealed that the maximum η_{th} was 30% without a cover and 70.6% with a cover. Similarly, the greatest η_{ex} was 17.8% without a cover and 26.1% with a cover, at a m_{air} of 0.03 kg s⁻¹. Azari et al. [58] conducted an evaluation in Zanjan, Iran, to determine how well a solar still combined with a V-groove solar collector performed. In comparison with the standard system, the upgraded one increased freshwater production by 170%, while yearly output exergy and energy were 257% and 170% higher, respectively. The η_{ex} of V down perforated baffled roughened SAH was found to be up to 76% higher in their study compared to the traditional models, according to Chamoli and Thakur [59]. Using two distinct roughness geometries (semicircular and square), Kumar et al. [60] examine how different factors affect the η_{ex} of a SAH. In comparison with a flat-plate SAH, the η_{ex} was enhanced drastically when roughness components were applied to the absorber plate. At lower Re , the square ribs η_{ex} remain almost 26% lesser than semicircular ribs. Velmurugan et al. [61] presented the

mathematical models to predict the η_{th} and η_{ex} of single, double, and triple pass (TPSAH). MATLAB was used to predict the performance, and it was inferred that, as the m_{air} increases, the η_{ex} increases and there is minimum rise in outlet air temperature; however, reverse happens in case of η_{ex} . It was also predicted that TPSAH performs better in comparison with double and single air pass in terms of η_{th} and η_{ex} . The results evaluated by mathematical models were collated with the findings by other studies and were in close agreement.

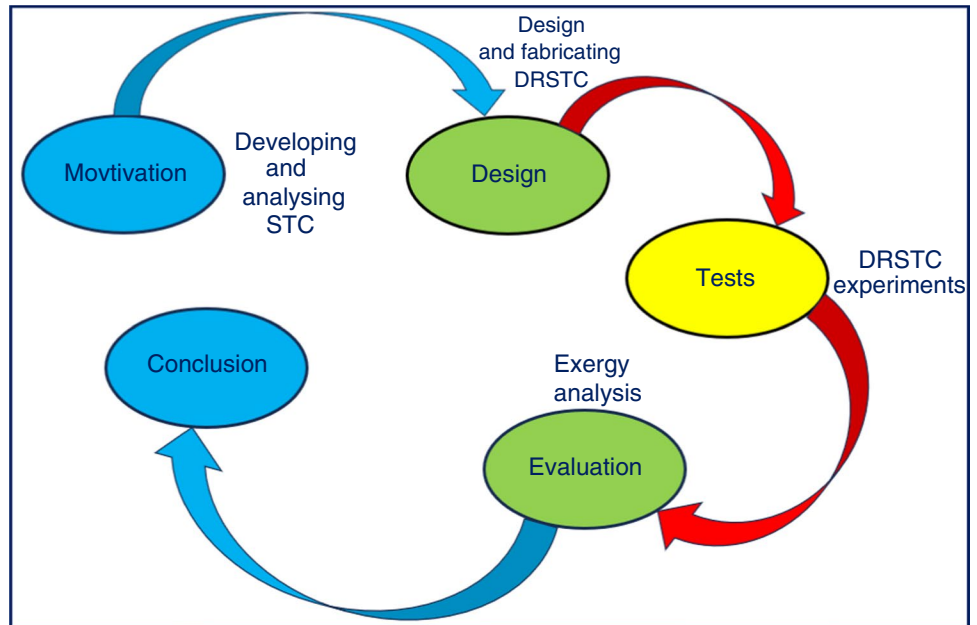
Based on the literature review, it was found that while considerable research has been conducted on roughened absorber STCs, the exergy analysis remains underexplored. Additionally, other roughened geometries for STCs have yet to receive sufficient attention. Few research on STC that employ artificial roughness have analyzed the η_{th} and η_{eff} of the STC system. Thus, using an analytical approach, the performance analysis of STC in conjunction with the novel arc-shaped dimple geometry is being investigated for the first time in this study. Therefore, this study's main goal and innovation are to utilize MATLAB for exergetic analysis to find the optimal roughness parameters based on previous experimental investigation [37].

Arc-shaped dimple forms placed strategically on the AP improve STC design efficiency by creating turbulence and reducing pressure drops along the channel's longitudinal axis. An iterative approach is used to assess the exergetic optimization of the STC for this arc-shaped dimple form type roughness. Large data sets containing more than two geometric parameters in a range of values are better suited for iterative techniques since they involve less computing work. If the iterative techniques provide an approximation result that is within a convergence limit, then it is acceptable. The goal of this technique is to reduce friction losses and increase the rate of HT in the air. As far as the author is aware, no research has been released that uses MATLAB to investigate the η_{ex} of an STC with arc-shaped dimple-type roughness on its AP. The flow chart for the current research is shown in Fig. 1.

Data collection and experimentation

A testing setup that has been created and built has been used to study the impact of the roughness component on Nu_{xx} and f_{xx} in a STC. The operational parameters and the system's practical elements are taken into consideration while determining the range of parameters. An arc-shaped dimple forms on the AP that is utilized to determine the η_{ex} of an STC, as shown in Fig. 2. During experimentation, the ranges of roughness parameters taken into consideration as e_d/D_h varied from 0.021 to 0.036 (0.021, 0.029, 0.036), p/e_d from 10 to 20 (10, 15, 20), and α_a from 45 to 75° (45°, 60°, 75°). Variations in Re_{xx} and roughness geometry parameters have

Fig. 1 Flow chart for the current investigation



been used to determine the statistical correlation between the Nu_{xx} and f_{xx} . Nu_{xx} and f_{xx} factor had maximum deviations of $\pm 8\%$ and $\pm 8\%$, respectively, in the range of parameters examined [37].

An illustration of the experimental apparatus is shown in the schematic form in Fig. 3. The air is drawn in by a 1.5 kW, three phase, 230 V, and 2820 rpm motor blower via a rectangular duct. The rectangular channel is divided into three sections: the entering segment, the test section, and the exit section. An entrance point on the rectangular duct lets in outside air. Joining the duct's leaving section to a circular galvanized iron pipe is the plenum, a rectangular mixing chamber. A calibrated orifice meter is attached to the circular pipe to measure the m_{air} . A U-tube manometer

is used to precisely measure the pressure difference that exists across the orifice meter. An aluminum AP comprises the test section of the rectangular duct. An array of dimples arranged in an arc pattern may be seen on the underside of the AP. Using an electric heater unit, the AP is heated. Heat is transferred from the heater assembly to the AP in a steady stream. The flow of heat is controlled by a variable transformer, often known as a variac. To determine the temperature of the heated roughened AP as well as the air in the surrounding area, a digital millivoltmeter and thermocouples made of copper constantan are used. A micro-manometer is used to measure the pressure difference in the test portion. The m_{air} that is contained inside the duct may be controlled with the assistance of

Fig. 2 Dimple shape in arc fashion

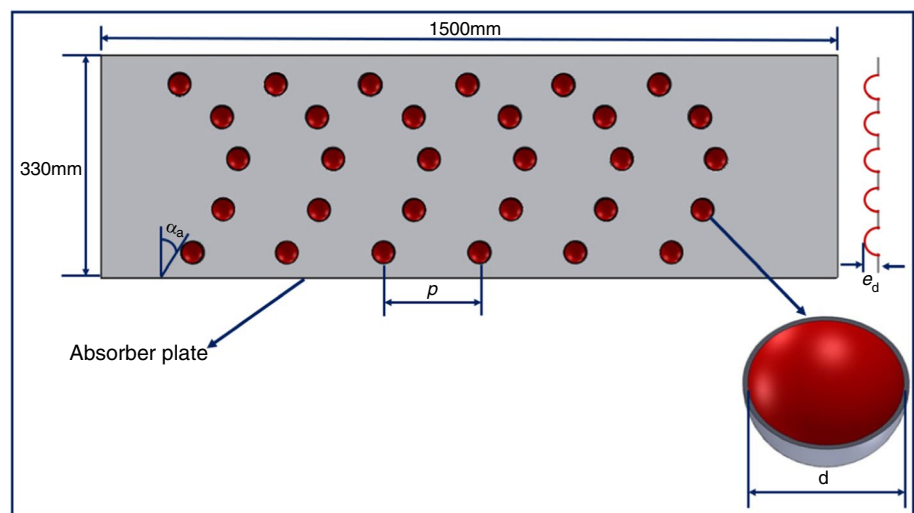
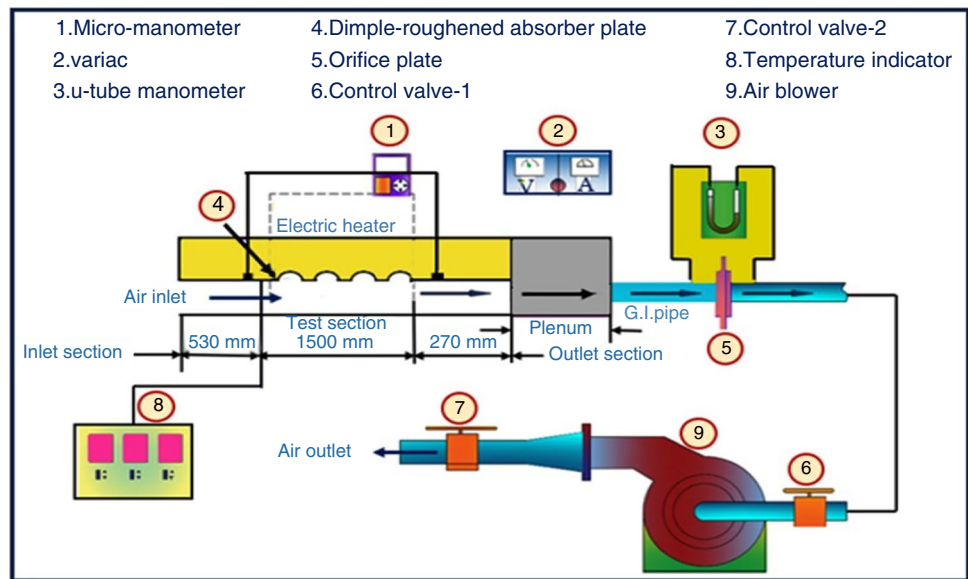


Fig. 3 Schematic diagram of experimental setup (STAC)



two control valves that are situated at the blower entrance and exit. As shown in Table 1, the accuracy and range of measuring instruments are presented.

$$f_{ss} = 0.085Re_{xx}^{-0.25} \tag{2}$$

Validity test for experimental setup

Before carrying out the experiment on roughened ducts, the test apparatus was validated by going through the process of performing tests on smooth channel. Based on the results of the experiments, the Nu_{ss} and the f_{ss} for smooth duct were calculated. After that, the values were compared with the values that were attained from the following correlation of the Dittus–Boelter equation for the Nu_{ss} and with the Modified Blasius equation for the f_{ss} for smooth channel. The maximum deviation for the Nu_{ss} and the f_{ss} was obtained to be ± 8.8 and $\pm 5.8\%$, respectively [37]. Figure 4a and b, respectively, compares the predicted values of the Nu_{ss} and the f_{ss} with the experimental outcomes.

Dittus–Boelter equation [62]

$$Nu_{ss} = 0.024Re_{xx}^{0.8}Pr^{0.4} \tag{1}$$

Modified Blasius equation [62]

Exergy-based analysis of DRSTC

The η_{ex} of a DRSTC is described as the ratio of net exergy flow (E_{nf}) to the associated exergy of solar irradiation (E_{sr}) received on the collector and expression for η_{ex} , as expressed in Eq. 3. STC is used in drying, space heating, and commercial activities. Many industries use exergy-based analysis for their complete system analysis, design, and optimization capabilities. This study focuses on improving absorber surfaces to maximize energy transfer to airflow while minimizing expenses. The 1st law of thermodynamics and an exergy-based study based on the 2nd law are often used to assess the effectiveness of DRSTC. The 2nd law of thermodynamics serves as the foundation for exergy analysis, which has been shown to be more logical than energy analysis. This is because exergy analysis concentrates on the origins, locations, and potential inefficiencies of thermal systems. The term exergy refers to the energy that exemplifies the maximum amount of work that can be accomplished without going against the principles of thermodynamics. Exergy is a quality that is possessed

Table 1 Accuracy and range of measurement instruments [24]

Instruments	Measurements	Range	Measurement accuracy
Micro-manometer	Pressure drops across test section	± 100 Pa	± 0.1 Pa
T-type thermocouples (Copper constantan)	Temperature of the roughened plate and air	0–400 °C	± 0.1 °C
U-tube manometer	Pressure drops across the orifice-plate	± 100 mm	± 1 mm
Vernier caliper	Dimensions of channel	0–150 mm	± 0.02 mm

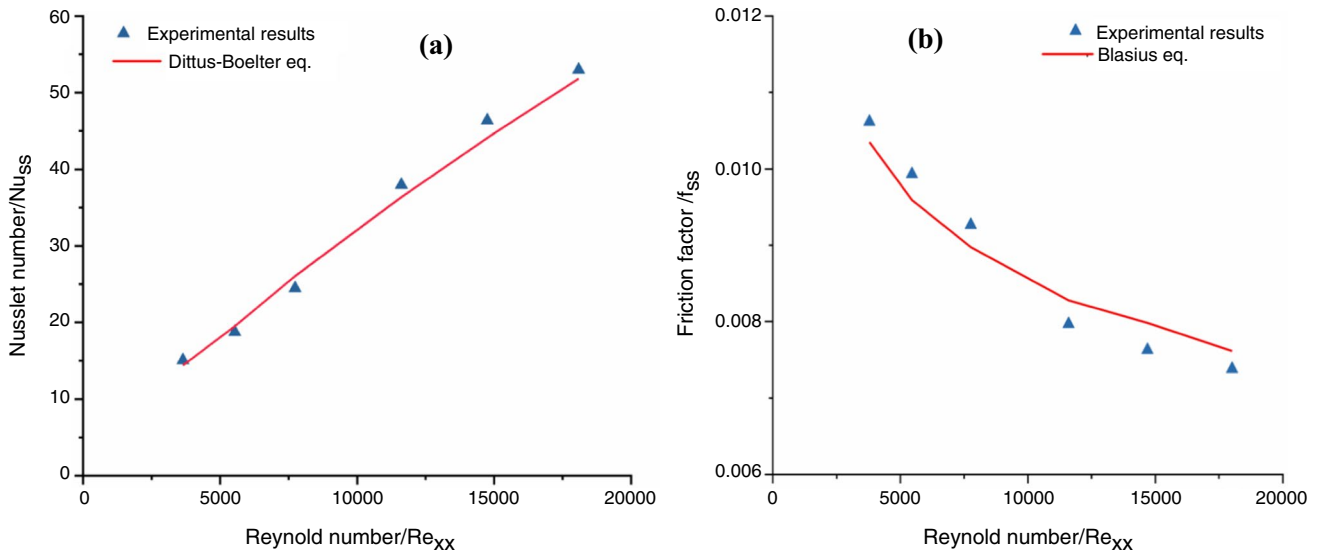


Fig. 4 Comparison of experimental and predicted values of **a** Nu_{ss} , and **b** f_{ss} for a smooth plate

by the combination of the system and the environment. Thermal devices such as STCs are more susceptible to the influence of the environment since the working fluid is air from the surrounding environment. When it comes to DRSTC, the term exergy refers to the greatest amount of heat that may be collected to heat up the surrounding air by using SE that is available. Furthermore, the exergy analysis is useful in evaluating the lost work potential, which is a measure of the amount of energy that has not been used.

$$\eta_{ex} = E_{nf}/E_{sr} \tag{3}$$

Altfeld et al. [63] created a model for determining the most effective parameters for air heaters. In the context of SAH, it was proposed that the application of mechanical power is necessary to overcome friction. In order to measure this, a parameter known as η_{ex} was established. This is determined by dividing the net exergy increase in air in the STC by the exergy flow caused by I_{sr} , which encompasses both the net exergy and the combined exergy losses due to radiation absorption. The net exergy flow, denoted as E_{nf} , is calculated by disregarding the variations in kinetic energy and potential energy and supposing air to be a perfect gas.

$$E_{nf} = I_{sr}A_p\eta_{th}\eta_c - P_m(1 - \eta_c) \tag{4}$$

I_{sr} is the global irradiation, A_p is plate (absorber) surface area, η_{th} is thermal efficiency [24]

P_m is pumping power, η_c is the Carnot efficiency, $\eta_c = (1 - \frac{T_{amb}}{T_f})$

The term E_{sr} refers to the exergy associated with the sun irradiation received on a collector. It is mathematically stated as:

$$E_{sr} = A_p I_{sr} \left(1 - \frac{T_{amb}}{T_s} \right) \tag{5}$$

where

T_s is the equivalent temperature of the sun as a black-body (≈ 5762 K).

The schematic diagrams of exergy flow as suggested by [63] for a SAH are represented in Fig. 5.

System and operating parameters

The performance analysis of an artificially roughened DRSTC requires the determination of fixed values for both the system and operating parameters. The system parameters include DRSTC duct dimensions that are used in the experimental work, namely L_t, W_d, H_d and roughness geometry parameters namely $e_d/D_h, p/e_d$ and α_a . The operating parameters are $T_{amb}, \mu_a, C_{pa}, k_{air}, \rho_a, V_w, \Delta T/I_{sr}$ or $[(T_o - T_i)/I_{sr}]$ and I_{sr} . The list of values suggested by [64] and many others is given in Table 2. Thermophysical characteristics were calculated as:

$$\mu_a = 1.81 \times 10^{-5} \left(\frac{T_f}{293} \right)^{0.735} \text{Ns m}^{-2} \tag{6}$$

$$C_{pa} = 1006 \left(\frac{T_f}{293} \right)^{0.0155} \text{J kg}^{-1}\text{K}^{-1} \tag{7}$$

Fig. 5 Schematic diagrams of exergy flow

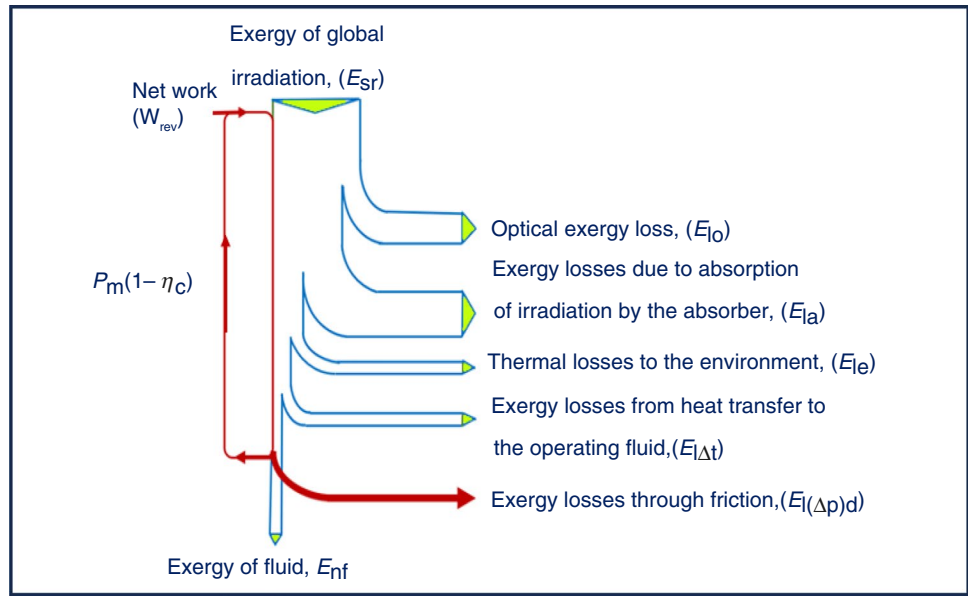


Table 2 System and operating parameters

Description		Parameter with units	Value/range		
System parameters	Fixed	L_t, m	1.5		
		W_d, m	0.33		
		H_d, m	0.030		
		$k_i, W m^{-1}K^{-1}$	0.037		
		t_i, m	0.024		
		$\tau\alpha$	0.85		
		N	1		
		ϵ_g	0.9		
		ϵ_p	0.88		
		t_g, m	0.002		
		L_g, m	0.025		
		t_e, m	0.040		
		Operating parameters	Fixed	T_{amb}, K	300
				$V_w, m s^{-1}$	1.0
$I_{sr}, W m^{-2}$	1000				
$\Delta T/I_{sr}$ or $[(T_o - T_i)/I_{sr}], Km^2W^{-1}$	0.003–0.02				
Operating parameters	Variable	e_d/D_h	10–20		
		$\alpha_a, ^\circ$	45–75		
		p/e_d	0.021–0.036		

$$k_{air} = 0.0275 \left(\frac{T_f}{293} \right)^{0.086} W m^{-1}K^{-1} \tag{8}$$

$$\rho_a = \frac{P_{atm}}{RT_f} Kg m^{-3} \tag{9}$$

Procedure for performance prediction

The prediction of DRSTC performance can be achieved by thoroughly analyzing the HT and fluid stream mechanisms within the system. The performance parameters that can be assessed include the U_l , F_r , and η_{ex} . This work has been conducted using a systematic and sequential procedure. The key characteristics of the process are outlined below:

1. Absorber plate's area is calculated by using Eq. 10:

$$A_p = W_{ap} \times L_{ap} \quad (10)$$

2. Diameter of the duct (Hydraulic) is calculated as:

$$D_h = (2W_d H_d) / (W_d + H_d) \quad (11)$$

3. The fixed system and operational parameters are taken as mentioned in Table 2.

4. A set of variable system roughness parameters is chosen in accordance with the information in Table 2.

5. A set of values of system and design operating parameters is selected as mentioned in Table 2.

6. The computation of the T_o and the temperature rise across the duct is as follows:

$$\Delta T = \frac{\Delta T}{I_{sr}} I_{sr} \quad (12)$$

$$T_o = T_i + \Delta T \quad (13)$$

7. Approximate initial T_p is taken as:

$$T_p = \frac{T_o + T_i}{2} + 10^\circ C \quad (14)$$

8. By employing the value of T_p , the value of the U_t is calculated from Eq. (15) given by [50].

$$U_t = \left(\frac{N}{\frac{C}{T_p} \left[\frac{(T_p - T_{amb})}{(N+f)} \right]^e + \frac{1}{h_w}} \right)^{-1} + \frac{\sigma(T_p^2 + T_{amb}^2)(T_p + T_{amb})}{(\epsilon_p + 0.00591N h_w)^{-1} + \frac{(2N+f-1+0.133\epsilon_p)}{\epsilon_g} - N} \quad (15)$$

where $h_w = 5.7 + 3.8V_w$, $f = (1 + 0.089h_w - 0.1166h_w\epsilon_p)(1 + 0.078660N)$
 $C = 520(1 - 0.000051\beta_{ta}^2)$ for $0^\circ < \beta_{ta} < 70^\circ$, using $\beta_{ta} = 70^\circ$, $e = 0.430(1 - 100/T_p)$ Other losses like U_b , U_e and U_l are also computed by using Eqs. (16, 17 and 18), respectively.

$$U_b = \frac{k_i}{t_i} \quad (16)$$

$$U_e = \frac{(L_t + W_d)t_e k_i}{L_t W_d t_i} \quad (17)$$

$$U_l = U_t + U_b + U_e \quad (18)$$

9. Rate of useful energy (\dot{Q}_{u1}) gain is determined as:

$$\dot{Q}_{u1} = [I_{sr}(\tau\alpha) - U_l(T_p - T_{amb})]A_p \quad (19)$$

The m_{air} is determined by using Eq. (20)

$$m_{air} = \frac{\dot{Q}_{u1}}{C_{pa} \Delta T} \quad (20)$$

10. Re_{xx} in the duct is computed as:

$$Re_{xx} = \frac{G_a D_h}{\mu_a} \quad (21)$$

where

$$G_a = \frac{m_{air}}{W_d H_d} \quad (22)$$

11. The Nu_{xx} is obtained by correlation developed [37] and reproduced below:

$$Nu_{xx} = 7.1 \times 10^{-3} \times Re_{xx}^{1.1386} \times (e_d/D_h)^{0.3629} \times (p/e_d)^{-0.047} \times (\alpha_a/60)^{-0.0048} \times \exp[-0.7792(\ln(\alpha_a/60))]^2 \quad (23)$$

12. Convective HT coefficient is computed as:

$$h_t = \frac{(Nu_{xx})k_{air}}{D_h} \quad (24)$$

13. The F' is then computed as:

$$F' = \frac{h_t}{h_t + U_l} \quad (25)$$

14. The F_r ; based on T_o , is calculated as:

$$F_r = \frac{m_{air} C_{pa}}{A_p U_l} \left[\exp \left\{ \frac{F' U_l A_p}{m_{air} C_{pa}} \right\} - 1 \right] \quad (26)$$

15. The new usable heat gain value is computed as follows:

$$\dot{Q}_{u2} = A_p F_r [I_{sr}(\tau\alpha) - U_l(T_o - T_i)] \quad (27)$$

16. When the differences between \dot{Q}_{u1} and \dot{Q}_{u2} are greater than 0.1% of \dot{Q}_{u1} , the new mean plate temperature value is computed as follows:

$$T_p = T_{amb} + [(I_{sr}(\tau\alpha) - \dot{Q}_{u2}/A_p)/U_l] \quad (28)$$

By employing this updated plate temperature value, the process from step 8 to step 16 is repeated until the disparity between \dot{Q}_{u1} and \dot{Q}_{u2} falls under the desired threshold. As a result:

$$\dot{Q}_u = \dot{Q}_{u1} = \dot{Q}_{u2}$$

- 17. The f_{xx} is obtained by correlation developed [37] and is reproduced below:

$$f_{xx} = 4.869 \times 10^{-1} \times (e_d/D_h)^{0.2663} \times Re_{xx}^{-0.223} \times (p/e_d)^{-0.059} \times (\alpha_a/60)^{0.0042} \times \exp[-0.4801(\ln(\alpha_a/60))]^2 \tag{29}$$

- 18. Making use of this value of f_{xx} , $(\Delta P)_d$ is calculated as:

$$(\Delta P)_d = \frac{4f_{xx}L_t\rho_aV_a^2}{2D_h} \tag{30}$$

- 19. The power needed to force air through the collector is computed as follows:

$$P_m = \frac{m_{air}(\Delta P)_d}{\rho_a} \tag{31}$$

- 20. Formula for logarithmic mean fluid temperature is:

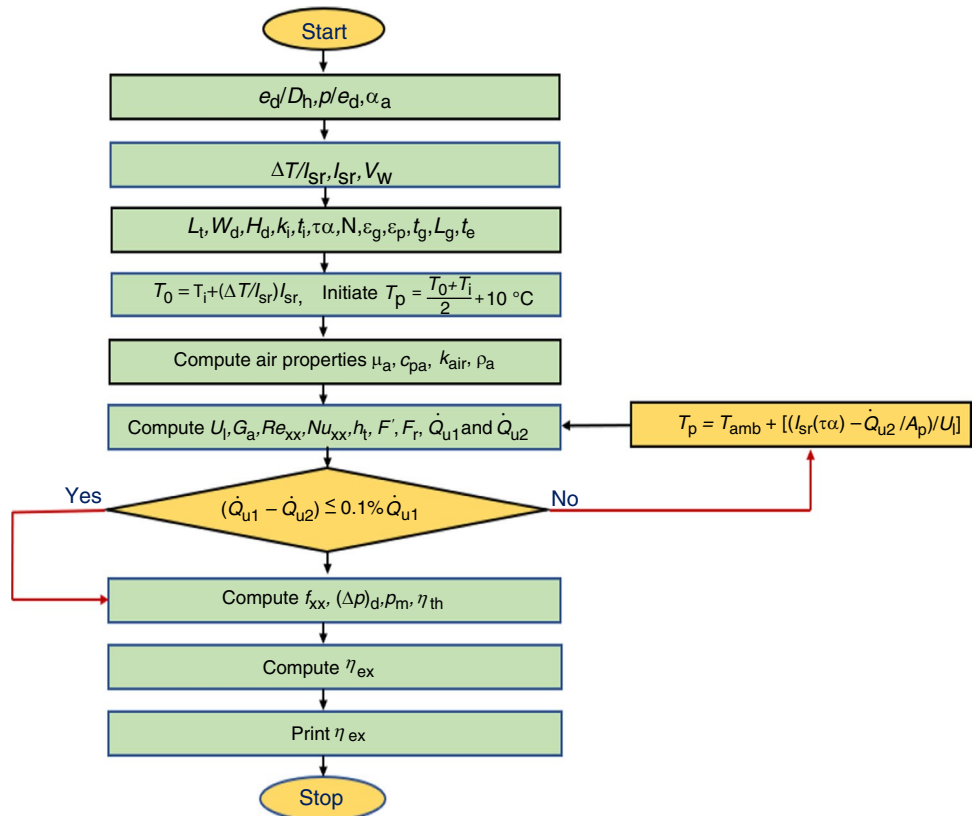
$$T_f = \frac{(T_o - T_i)}{\ln\left(\frac{T_o}{T_i}\right)} \tag{32}$$

- 21. Carnot efficiency, which can be computed using the logarithmic mean air temperature, is as follows:

$$\eta_c = 1 - \left(\frac{T_{amb}}{T_f}\right) \tag{33}$$

- 22. The net exergy flow to the air is computed by using Eq. (4).
- 23. Exergy input is calculated by using Eq. (5).
- 24. Exergetic efficiency is calculated by using Eq. (3).
- 25. Next set of values of $\Delta T/I_{sr}$ is chosen, and steps 4–24 are repeated to cover the range of $\Delta T/I_{sr}$.
- 26. The next set of roughness geometry parameters, which include e_d/D_h , p/e_d , and α_a are chosen, and then steps 4 to 25 are carried out once again. A computer program is run in MATLAB (R2023a) to find the values of various efficiencies of artificially roughened DRSTC channel. Figure 6 illustrates the flow diagram for the program.

Fig. 6 Computer program’s flowchart



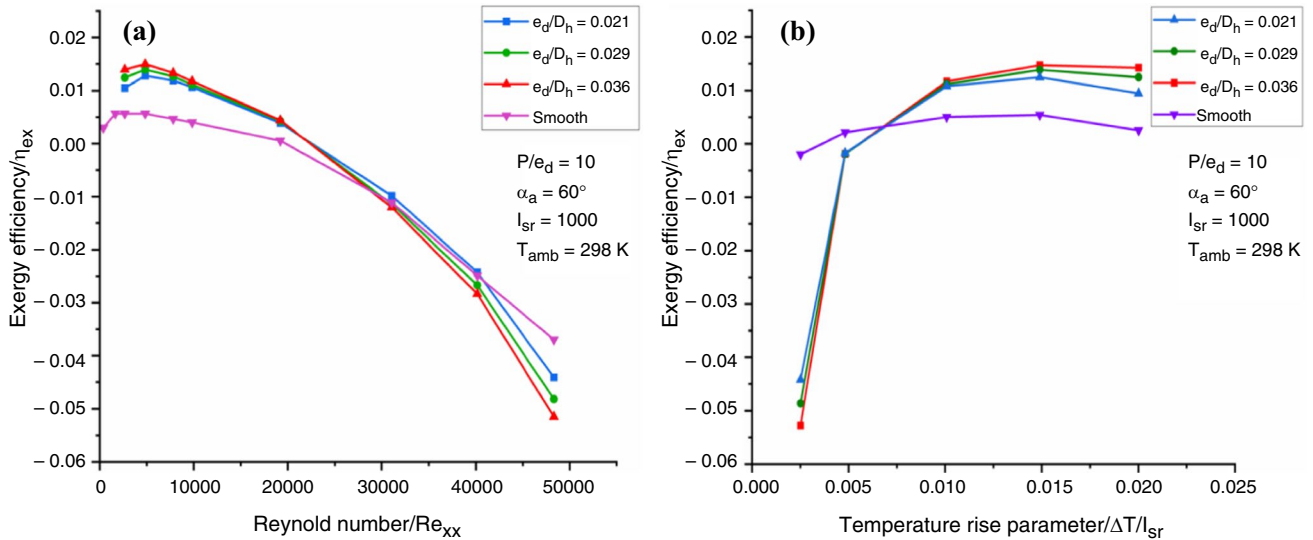


Fig. 7 Influence of e_d/D_h on η_{ex} as a function of **a** Re_{xx} , **b** $\Delta T/I_{sr}$

Results and discussion

An analysis of the η_{ex} has been performed as a function of Re_{xx} and $\Delta T/I_{sr}$ which include all the system and operational characteristics that are listed in Table 2. The variability of η_{ex} with Re_{xx} is shown in Fig. 7a. This variation is seen for e_d/D_h values of 0.021, 0.029, and 0.036, as well as for a fixed value of $p/e_d = 10$ and $\alpha_a = 60^\circ$. The highest value of η_{ex} corresponds to a e_d/D_h value of 0.036, and it has been found that the value of η_{ex} rises with a rise in the e_d/D_h value when the Re_{xx} is up to around 6000. When the Re_{xx} is increased above this value, the tendency begins to reverse.

The variation of η_{ex} with $\Delta T/I_{sr}$ for e_d/D_h values of 0.021, 0.029, and 0.036, as well as for fixed values of $p/e_d = 10$ and $\alpha_a = 60^\circ$, is illustrated in Fig. 7b.

It has been observed that the η_{ex} improves with an increase in e_d/D_h for $\Delta T/I_{sr}$ values that are more than $0.0087 \text{ Km}^2 \text{ W}^{-1}$. On the other hand, this tendency is reversed for $\Delta T/I_{sr}$ values that are lower than $0.0087 \text{ Km}^2 \text{ W}^{-1}$. When compared to DRSTC, the performance of smooth conventional STC is superior when the $\Delta T/I_{sr}$ value is below $0.0065 \text{ Km}^2 \text{ W}^{-1}$. On the other hand, when the $\Delta T/I_{sr}$ value falls within the range of $0.0065\text{--}0.0072 \text{ Km}^2 \text{ W}^{-1}$, e_d/D_h value of 0.021 yields the highest possible value of η_{ex} . For $\Delta T/I_{sr}$ values ranging from 0.0072 to $0.0087 \text{ Km}^2 \text{ W}^{-1}$, the

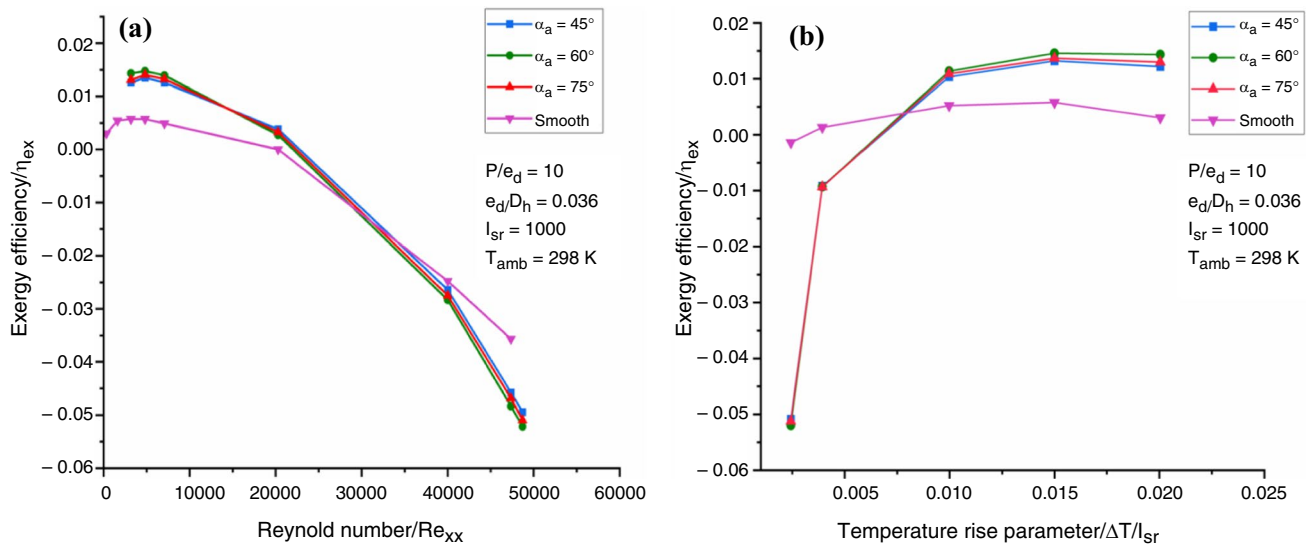


Fig. 8 Influence of α_a on η_{ex} as a function of **a** Re_{xx} , **b** $\Delta T/I_{sr}$

highest possible value of η_{ex} is achieved with e_d/D_h value of 0.029. However, when the $\Delta T/I_{sr}$ value exceeds 0.0087, the highest possible value of η_{ex} is achieved with a e_d/D_h value of 0.036. In Fig. 8a, the variation in η_{ex} with Re_{xx} is shown for α_a values of 45°, 60°, and 75°, as well as for fixed value of $e_d/D_h = 0.036$ and $p/e_d = 10$. For Re_{xx} values that are lower than 22,000, the highest value of η_{ex} is achieved by using an α_a value of 60°. Conversely, for Re_{xx} that fall within the range of 22,000 to 25,000, the maximum value of η_{ex} is achieved by utilizing an α_a of 45°. The greatest value of η_{ex} is achieved for α_a of 75° when the Re_{xx} is between 25,000 and 44,000, and it corresponds to a smooth STC when the Re_{xx} is higher than 44,000. The η_{ex} of a particular arc angle improves with an increase in the Re_{xx} until it reaches its highest value, after which it begins to decline with additional rise in the Re_{xx} value.

Figure 8b illustrates the variation in η_{ex} as a function of the $\Delta T/I_{sr}$ for α_a value of 45°, 60°, and 75°, as well as for fixed values of $e_d/D_h = 0.036$ and $p/e_d = 10$. When the $\Delta T/I_{sr}$ value is less than 0.0055 Km^2W^{-1} , smooth STC performs better than DRSTC. On the other hand, when the $\Delta T/I_{sr}$ value is larger than 0.0068 Km^2W^{-1} , the α_a value of 60° has the best performance in comparison with other values of α_a . For $\Delta T/I_{sr}$ value in the range of 0.0055–0.0061 Km^2W^{-1} , α_a value of 45° yields the highest value of η_{ex} and for $\Delta T/I_{sr}$ value in the range of 0.0061–0.0068 Km^2W^{-1} , the uppermost value of η_{ex} corresponds to α_a value of 75°. Figure 9a illustrates the variation of η_{ex} with Re_{xx} for p/e_d of 10, 15, 20 and for a fixed value of $e_d/D_h = 0.036$ and $\alpha_a = 60^\circ$. The utmost value of η_{ex} is achieved by smooth STC when the Re_{xx} value is larger than 42,000. Conversely, when the Re_{xx} value is less than 20,000, the p/e_d value of 10 is

effective in producing the highest possible value of η_{ex} . The maximum values of η_{ex} for Re_{xx} ranges of 20,000–23,000 and 23,000–42,000 are computed based on p/e_d values of 15 and 20, respectively. These values correlate to the maximum values of η_{ex} .

Figure 9b illustrates the variation of η_{ex} with $\Delta T/I_{sr}$ for p/e_d values of 10, 15, 20 and for a fixed value of $e_d/D_h = 0.036$ and $\alpha_a = 60^\circ$. It has been observed that smooth STC performs better than DRSTC when the $\Delta T/I_{sr}$ value is less than 0.0054 Km^2W^{-1} . On the other hand, when the $\Delta T/I_{sr}$ value is greater than 0.0071 Km^2W^{-1} , the p/e_d value of 10 yields the highest possible value of η_{ex} . When the $\Delta T/I_{sr}$ value falls within the range of 0.0054–0.0060 Km^2W^{-1} , the maximum value of η_{ex} is attained for a p/e_d value of 20. On the other hand, when the $\Delta T/I_{sr}$ value falls within the range of 0.0060–0.0071 Km^2W^{-1} , the maximum value is obtained for a p/e_d value of 15. In the case of a certain value of p/e_d , the η_{ex} rises as the $\Delta T/I_{sr}$ is increased, reaches its highest possible value, and then begins to fall as the $\Delta T/I_{sr}$ is increased even more. The parameters related to roughness geometry values that outcome in the highest possible value of η_{ex} are presented in Tables 3 and 4. These tables include the results for various ranges of the Re_{xx} and the $\Delta T/I_{sr}$, respectively, which correspond to an I_{sr} value of 1000 Wm^{-2} . It is evident that there is no one value or set of roughness geometry parameters that may provide the highest possible η_{ex} throughout the whole range of Re_{xx} or $\Delta T/I_{sr}$.

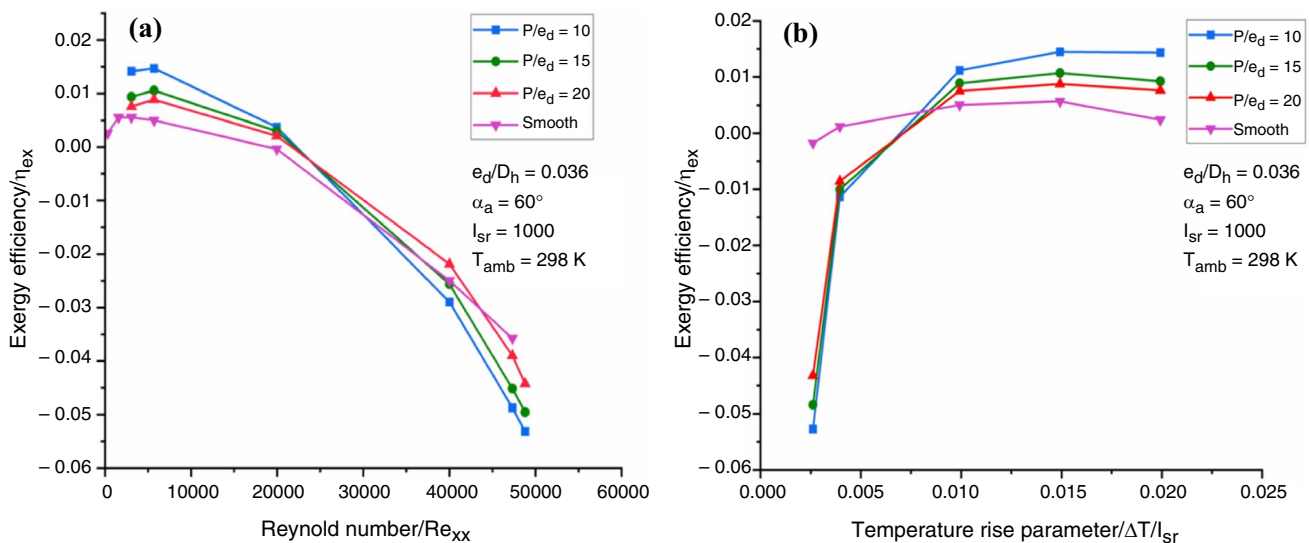


Fig. 9 Influence of p/e_d on η_{ex} as a function of a Re_{xx} , b $\Delta T/I_{sr}$

Table 3 Re_{xx} range corresponding to highest η_{ex} ($I_{sr} = 1000 \text{ Wm}^{-2}$)

Roughness parameter	Fixed parameter	Re_{xx} range	Value of roughness parameter
Relative roughness height (e_d/D_h)	$p/e_d = 10$ $\alpha_a = 60^\circ$	$Re_{xx} < 19,000$	0.036
		$19,000 < Re_{xx} < 19,600$	0.029
		$19,600 < Re_{xx} < 42,500$	0.021
		$Re_{xx} > 42,500$	Smooth
Arc angle (α_a)	$e_d/D_h = 0.036$ $p/e_d = 10$	$Re_{xx} < 22,000$	60°
		$22,000 < Re_{xx} < 25,000$	45°
		$25,000 < Re_{xx} < 44,000$	75°
		$Re_{xx} > 44,000$	Smooth
Relative roughness pitch (p/e_d)	$e_d/D_h = 0.036$ $\alpha_a = 60^\circ$	$Re_{xx} < 20,000$	10
		$20,000 < Re_{xx} < 23,000$	15
		$23,000 < Re_{xx} < 42,000$	20
		$Re_{xx} > 42,000$	Smooth

Table 4 $\Delta T/I_{sr}$ range corresponding to highest η_{ex} ($I_{sr} = 1000 \text{ Wm}^{-2}$)

Roughness parameter	Fixed parameter	$\Delta T/I_{sr}$ range (Km^2W^{-1})	Value of roughness parameter
Relative roughness height (e_d/D_h)	$p/e_d = 10$ $\alpha_a = 60^\circ$	$\Delta T/I_{sr} < 0.0065$	Smooth
		$0.0065 < \Delta T/I_{sr} < 0.0072$	0.021
		$0.0072 < \Delta T/I_{sr} < 0.0087$	0.029
		$\Delta T/I_{sr} > 0.087$	0.036
Arc angle (α_a)	$e_d/D_h = 0.036$ $p/e_d = 10$	$\Delta T/I_{sr} < 0.0055$	Smooth
		$0.0055 < \Delta T/I_{sr} < 0.0061$	45°
		$0.0061 < \Delta T/I_{sr} < 0.0068$	75°
		$\Delta T/I_{sr} > 0.0068$	60°
Relative roughness pitch (p/e_d)	$e_d/D_h = 0.036$ $\alpha_a = 60^\circ$	$\Delta T/I_{sr} < 0.0054$	Smooth
		$0.0054 < \Delta T/I_{sr} < 0.0060$	20
		$0.0060 < \Delta T/I_{sr} < 0.0071$	15
		$\Delta T/I_{sr} > 0.0071$	10

Conclusions

Based on the existing correlations, the exergetic performance of DRSTC has been analytically examined with respect to the roughness (e_d/D_h , α_a , and p/e_d) and operational parameters ($\Delta T/I_{sr}$ and I_{sr}) of the DRSTC. The following findings were reached considering the present work outcomes:

- Exergetic efficiency has been used to assess DRSTC performance, and it has been determined that the greatest value of η_{ex} is obtained when the e_d/D_h value of 0.021 is obtained, with the $\Delta T/I_{sr}$ value falling between 0.0065 and 0.0072 Km^2W^{-1} . For $\Delta T/I_{sr}$ values ranging from 0.0072 to 0.0087 Km^2W^{-1} , the highest possible value of η_{ex} is achieved with a e_d/D_h value of 0.029. However, when the $\Delta T/I_{sr}$ value exceeds 0.0087, the highest possible value of η_{ex} is achieved with a e_d/D_h value of 0.036.
- On the basis of η_{ex} , it was discovered that when the $\Delta T/I_{sr}$ value is larger than 0.0068 Km^2W^{-1} , the α_a value of 60° has the highest performance when compared to other values of α_a . When the $\Delta T/I_{sr}$ value falls within the range of 0.0055–0.0061 Km^2W^{-1} , the highest value of η_{ex} is obtained by utilizing an α_a value of 45° . Conversely, when the $\Delta T/I_{sr}$ value falls within the range of 0.0061–0.0068 Km^2W^{-1} , the highest value of η_{ex} corresponds to an α_a value of 75° .
- Exergetic efficiency revealed that the highest value of η_{ex} may be achieved with a p/e_d value of 10, provided that the $\Delta T/I_{sr}$ value is more than 0.0071 Km^2W^{-1} . The greatest value of η_{ex} is found for a p/e_d value of 20, while the $\Delta T/I_{sr}$ value is between 0.0054 and 0.0060 Km^2W^{-1} . Conversely, a p/e_d value of 15 yields the

greatest result when the $\Delta T/I_{sr}$ value is between 0.0060 and 0.0071 Km^2W^{-1} .

Future scope and implications

This article provides a thorough investigation of the exergetic efficiency of an STC with arc-shaped dimples forming on its absorber surface. According to the study, the optimized STC configuration achieves the maximum $\eta_{ex} = 1.47\%$ with a $\Delta T/I_{sr}$ of 0.0071 Km^2W^{-1} , which is necessary to attain the optimal values of $e_d/D_h = 0.036$, $p/e_d = 10$, and $\alpha_a = 60^\circ$. These findings have significant implications for different stakeholders: Industry professionals can use the optimized design parameters to improve STC efficiency; policy-makers can use the information to support renewable energy policies; and investigators have the option to use performance analysis and the methodological approach as a basis for future innovation in SE systems. In general, this study advances solar thermal technology, encourages wider use of it, and aids in achieving international energy sustainability targets. Additionally, the research highlights how crucial it is for practical implementation to use prototyping, thorough testing, and scalable designs that can be adjusted to various climates and uses. To improve on the existing results and further the field, future studies on STCs with dimple shape should concentrate on addressing many important issues. By strengthening the AP capacity to absorb and hold SE, selective coatings-like carbon-based compounds or black chrome improve the system's thermal performance. Moreover, adding nanoparticles to the AP material may improve thermal conductivity even more, resulting in quicker and more even heat dispersion. Furthermore, the application of multicriteria decision-making based methodologies for STC optimization will enable the determination of optimal parameters for maximizing STC efficiency with coated AP.

Author contributions Raj Kumar contributed to Conceptualization, Methodology, Validation, Data curation, Software, Visualization, Writing—original draft, and Writing—review and editing. Muneesh Sethi contributed to Conceptualization, Methodology, Validation, Data curation, Software, Visualization, Writing—original draft, and Writing—review and editing. Abhishek Thakur contributed to Methodology, Data curation, Software, and Writing—review and editing. Adit Rana contributed to Methodology, Data curation, and Writing—review and editing. Varun Goel contributed to Methodology, Data curation, and Writing—review and editing. Daeho Lee contributed to Conceptualization, Methodology, Validation, Visualization, and Writing—review and editing. Tej Singh contributed to Conceptualization, Methodology, Validation, Visualization, and Writing—review and editing.

Funding Open access funding provided by Eötvös Loránd University.

Open Access This article is licensed under a Creative Commons Attribution 4.0 International License, which permits use, sharing,

adaptation, distribution and reproduction in any medium or format, as long as you give appropriate credit to the original author(s) and the source, provide a link to the Creative Commons licence, and indicate if changes were made. The images or other third party material in this article are included in the article's Creative Commons licence, unless indicated otherwise in a credit line to the material. If material is not included in the article's Creative Commons licence and your intended use is not permitted by statutory regulation or exceeds the permitted use, you will need to obtain permission directly from the copyright holder. To view a copy of this licence, visit <http://creativecommons.org/licenses/by/4.0/>.

References

1. Mund C, Rathore SK, Sahoo RK. Analysis of solar air heaters based on computational fluid dynamics. *J Therm Anal Calorim.* 2024;149:1831–57.
2. Bharadwaj G, Sharma K, Pandey AK, Gupta A. Carbon nanotube–graphene-based nanofluids: a comprehensive review on the role of thermal conductivity and its solar energy applications. *J Therm Anal Calorim.* 2024;149:1859–93.
3. Abdelrazik AS, Osama A, Allam AN, Shboul B, Sharafeldin MA, Elwardany M, Masoud AM. ANSYS-Fluent numerical modeling of the solar thermal and hybrid photovoltaic-based solar harvesting systems. *J Therm Anal Calorim.* 2023;148:11373–424.
4. Singh H, Kishore C, Chamoli S, Joshi A. Enhancing heat transfer in rectangular solar air heater channels: a numerical exploration of multiple Boomerang-shaped roughness elements with variable gaps. *Energy Sour, Part A: Recover, Util, Environ Eff.* 2024;46:6696–712.
5. Bhattacharyya S, Pathak M, Sharifpur M, Chamoli S, Ewim DRE. Heat transfer and exergy analysis of solar air heater tube with helical corrugation and perforated circular disc inserts. *J Therm Anal Calorim.* 2021;145:1019–34.
6. Chaudhri K, Bhagoria JL, Kumar V. Heat transfer and friction factor correlation for rhombus-shaped roughness geometry on the absorber plate of solar air collector. *J Therm Anal Calorim.* 2024;149:6405–20.
7. Duarte RMD, Salviano LO, Ferreira WG, Dezan DJ. Numerical investigation of heat transfer enhancement by using louvered-winglet vortex generators mounted in a solar air heater channel-type. *J Therm Anal Calorim.* 2023;148:14183–204.
8. Kumar A, Layek A. Thermo-hydraulic performance of solar air heater having winglet type roughness element. *J Therm Anal Calorim.* 2022;147:10481–95.
9. Singh H, Kishore C, Chamoli S, Bhattacharya S. Enhancing heat transfer in heat exchanger tube using four-shape cutting cone (FSCC) inserts: a numerical analysis. *Energy Sour, Part A: Recover, Util, Environ Eff.* 2024;46(1):52–74.
10. Singh T. Entropy weighted WASPAS and MACBETH approaches for optimizing the performance of solar water heating system. *Case Stud Therm Eng.* 2024;53: 103922.
11. Bahuguna R, Mer KKS, Kumar M, Chamoli S. Thermohydraulic performance and second law analysis of a tube embedded with multiple helical tape inserts. *Energy Sour, Part A: Recover, Util, Environ Eff.* 2021. <https://doi.org/10.1080/15567036.2021.1904057>.
12. Yadav AK, Yadav V, Kumar A, Kumar R, Lee D, Singh T. Novel feature selection-based ANN for optimal solar panels tilt angles prediction in micro grid. *Case Stud Therm Eng.* 2024;61: 104853.
13. Kumar S, Thakur R, Kumar S, Lee D, Kumar R. Impact of liquid spectrum filter and solar tracker on the overall effectiveness

- of a photovoltaic thermal system: an experimental investigation. *Renew Energy*. 2024;226: 120390.
14. Khargotra R, Kumar R, Kovács A, Singh T. Techno-economic analysis of solar thermal collector for sustainable built environment. *J Therm Anal Calorim*. 2023;149:1175–84.
 15. Kumar S, Kumar R, Thakur R, Kumar S, Lee D. Effects of climate variables and nanofluid-based cooling on the efficiency of a liquid spectrum filter-based concentrated photovoltaic thermal system. *J Therm Anal Calorim*. 2024;149:2273–91.
 16. Khargotra R, Kumar S, Singh T, Lee D, Kumar R. Correlation proposing and ANN modeling of thermo-hydraulic performance for delta shaped winglets type solar water heating system. *J Therm Anal Calorim*. 2024;149:6459–81.
 17. Aggarwal S, Kumar R, Kumar S, Singh T. Impact of fin material properties and the inclination angle on the thermal efficiency of evacuated tube solar water heater: an experimental study. *J King Saud Univer - Sci*. 2024;36: 103186.
 18. Aggarwal S, Kumar R, Lee D, Kumar S, Singh T. A comprehensive review of techniques for increasing the efficiency of evacuated tube solar collectors. *Heliyon*. 2023;9: e15185.
 19. Kumar R, Sharma N, Chahat NGH, Yadav AK, Lee D, Singh T. Prediction of jet impingement solar thermal air collector thermohydraulic performance using soft computing techniques. *Case Stud Therm Eng*. 2024;55:04144.
 20. Thakur A, Kumar R, Lee D, Kumar S, Asif M, Ağbulut Ü. Improved performance evaluation of a dual passage solar thermal collector using staggered turbulators. *Therm Sci Eng Progr*. 2024;53: 102668.
 21. Kumar R, Lee D, Kumar S, Thapa S, Gürel AE, Thakur A, Jilte RD, Saleel CA, Shaik S, Ağbulut Ü. Different energy storage techniques: recent advancements, applications, limitations and efficient utilization of sustainable energy. *J Therm Anal Calorim*. 2024;149:1895–933.
 22. Kumar R, Kumar S, Ağbulut Ü, Gürel AE, Alwetaishi M, Shaik S, Saleel CA, Lee D. Parametric optimization of an impingement jet solar air heater for heater for active green heating in buildings using hybrid CRITIC-COPRAS approach. *Int J Therm Sci*. 2024;197: 108760.
 23. Alkhalaf Q, Lee D, Kumar R, Thapa S, Singh AR, Akhtar MN, Asif M, Ağbulut Ü. Experimental investigation of the thermal efficiency of a new cavity receiver design for concentrator solar technology. *Case Stud Therm Eng*. 2024;53: 103848.
 24. Kumar R, Sethi M, Goel V, Ramis MK, AlSubih M, Islam S, Ansari MSA, Lee D, Wodajo AW. Thermal and effective assessment of solar thermal air collector with roughened absorber surface: an analytical examination. *Int J Low Carbon Technol*. 2024;19:1112–23.
 25. Thapa S, Kumar R, Lee D. Energetic and exergetic analysis of jet impingement solar thermal collector featuring discrete multi-arc shaped ribs absorber surface. *Energy*. 2024;306: 132392.
 26. Chauhan R, Kim SC. Effective efficiency distribution characteristics in protruded/dimpled arc plate solar thermal collector. *Renew Energy*. 2019;138:955–63.
 27. Alrashidi A, Altohamy AA, Abdelrahman MA, Elsemary MMI. Energy and exergy experimental analysis for innovative finned plate solar air heater. *Case Stud Therm Eng*. 2024;59: 104570.
 28. Sharma A, Pitchumani R, Chauhan R. Melting and solidification performance investigation of latent heat storage unit designs for low-temperature solar thermal applications. *J Energy Storage*. 2023;66: 107323.
 29. Arunkumar HS, Shiva Kumar K, Karanth V. Energy exergy and economic analysis of a multiple inlet solar air heater for augmented thermohydraulic performance. *Appl Therm Eng*. 2024;246:122981. <https://doi.org/10.1016/j.applthermaleng.2024.122981>.
 30. Chauhan R, Kim SC. Thermo-hydraulic characterization and design optimization of dimpled/protruded absorbers in solar heat collectors. *Appl Therm Eng*. 2019;154:217–27.
 31. Kushwaha PK, Kumar A, Choudhary R. Energy, exergy, economic, and environmental (4-E) analysis of atmospheric water harvesting system based on desiccant wheel using solar air heater. *J Water Process Eng*. 2024;62: 105377.
 32. Chamoli S, Chauhan R, Thakur NS. Numerical analysis of heat transfer and thermal performance analysis of surface with circular profile fins. *Int J Energy Sci*. 2011;1(1):11–8.
 33. Bhattacharyya S, Benim AC, Pathak M, Chamoli S, Gupta A. Thermohydraulic characteristics of inline and staggered angular cut baffle inserts in the turbulent flow regime. *J Therm Anal Calorim*. 2020;140:1519–36.
 34. Sharma A, Ding C, Kim SC, Chauhan R. Investigation and optimization of solidification performance of concentration tube type latent heat storage unit with herringbone wavy fin designs. *Appl Therm Eng*. 2023;222:119924.
 35. Fattoum R, Hidouri A, Attia MEH, Arıcı M, Abbassi MA. Optimization of solar air heaters performance using parallel porous wire mesh: energy, exergy, and enviro-economic analyses. *Therm Sci Eng Progr*. 2024;48: 102385.
 36. Pachori H, Choudhary T, Sheorey T, Shukla AK, Verma V. A novel energy, exergy and sustainability analysis of a decentralized solar air heater integrated with V-shaped artificial roughness for solar thermal application. *Sustain Energy Technol Assess*. 2024;66: 103816.
 37. Sethi M, Varun NST. Correlations for solar air heater duct with dimpled shape roughness elements on absorber plate. *Sol Energy*. 2012;86(9):2852–61. <https://doi.org/10.1016/j.solener.2012.06.024>.
 38. Kumar A, Kumar R, Bhushan A. Differential exergy investigation and environ-economic assessment of a dimpled plate and flat plate solar air heater under turbulent conditions. *Appl Therm Eng*. 2024;240: 122299.
 39. Bhuvad SS, Rizvi IH, Azad R. Apex-up discrete-arc rib roughened solar air heater- energy and exergy based experimental study. *Sol Energy*. 2023;25:362–78.
 40. Nidhul K, Yadav AK, Anish S, Arunachala US. Efficient design of an artificially roughened solar air heater with semicylindrical side walls: CFD and exergy analysis. *Sol Energy*. 2020;207:289–304.
 41. Luan NT, Phu NM. Thermohydraulic correlations and exergy analysis of a solar air heater duct with inclined baffles. *Case Stud Therm Eng*. 2020;21: 100670.
 42. Thapa S, Kumar R, Kumar K, Samir S, Lee D, Singh T. Analytical investigation of solar parabolic trough receiver with multiple twisted tapes using exergy and energy analysis. *Case Stud Therm Eng*. 2023;50: 103493.
 43. Harikrishnan M, Kumar RA, Baby R, Percy D, Kumar SA. Exergetic performance assessment of a downward solar air heater with impinging air jets: an experimental study. *Case Stud Therm Eng*. 2024;55: 104104.
 44. Mortazavi A, Ameri M. Conventional and advanced exergy analysis of solar flat plate air collectors. *Energy*. 2018;142:277–88.
 45. Nidhul K, Kumar S, Yadav AK, Anish S. Enhanced thermohydraulic performance in a V-ribbed triangular duct solar air heater: CFD and exergy analysis. *Energy*. 2020;200: 117448.
 46. Hassan H, Osman OO, Abdelmoez MN, Abo-Elfadl S. Energy and exergy evaluation of new design nabla shaped tubular solar air heater (V TSAH): experimental investigation. *Energy*. 2023;276: 127451.
 47. Kumar PG, Vigneswaran VS, Balaji K, Vinothkumar S, Prabakaran R, Sakthivadivel D, Meikandan M, Kim SC. Augmented V-corrugated absorber plate using shot-blasting for solar air heater: energy, exergy, economic, and environmental (4E) analysis. *Process Saf Environ Prot*. 2022;165:514–31.

48. Abdelkader TK, Zhang Y, Gaballah ES, Wang S, Wan Q, Fan Q. Energy and exergy analysis of a flat-plate solar air heater coated with carbon nanotubes and cupric oxide nanoparticles embedded in black paint. *J Clean Prod.* 2020;250: 119501.
49. Khanlari A, Tuncer AD, Sozen A, Aytaç I, Çiftçi E, Variyenli HI. Energy and exergy analysis of a vertical solar air heater with nano-enhanced absorber coating and perforated baffles. *Renew Energy.* 2022;187:586–602.
50. Hegde AK, Pai R, Karanth KV. Energy and exergy analysis of a cross flow solar air heater for thermohydraulic performance augmentation. *Int J Therm Sci.* 2023;194: 108577.
51. Ghiami A, Ghiami S. Comparative study based on energy and exergy analyses of a baffled solar air heater with latent storage collector. *Appl Therm Eng.* 2018;133:797–808.
52. Avargani VM, Zendejboudi S, Rahimi A, Soltani S. Comprehensive energy, exergy, enviro-exergy, and thermo-hydraulic performance assessment of a flat plate solar air heater with different obstacles. *Appl Therm Eng.* 2022;203: 117907.
53. Sharma A, Chauhan R. Integrated and separate collector storage type low-temperature solar water heating systems with latent heat storage: a review. *Sustain Energy Technol Assess.* 2022;51: 101935.
54. Abo-Elfadl S, El-Dosoky MF, Hassan H. Energy and exergy assessment of new designed solar air heater of V-shaped transverse finned absorber at single and double-pass flow conditions. *Environ Sci Pollut Res.* 2021;28:69074–92.
55. Singh I, Vardhan S. Energy, exergy, environmental and economic (4E) analysis of evacuated tube solar collector with helical coils. *J Mech Sci Technol.* 2022;36:5801–8.
56. Abo-Elfadl S, Yousef MS, Hassan H. Assessment of double-pass pin finned solar air heater at different air mass ratios via energy, exergy, economic, and environmental (4E) approaches. *Environ Sci Pollut Res.* 2021;28:13776–89.
57. Reddy SVK, Venkateswarlu K, Akram F, Prasanth A, Patrick A, Ahmed N, Panicker S, Shariff T. Energy and exergy analyses of plastic solar air heater developed from chlorinated polyvinyl chloride pipes. *Appl Solar Energy.* 2023;59:943–56.
58. Azari P, Lavasani AM, Rahbar N, Yazdi ME. Performance enhancement of a solar still using a V-groove solar air collector-experimental study with energy, exergy, enviroeconomic, and exergoeconomic analysis. *Environ Sci Pollut Res.* 2021;28:65525–48.
59. Chamoli S, Thakur NS. Exergetic performance evaluation of solar air heater having V-down perforated baffles on the absorber plate. *J Therm Anal Calorim.* 2014;117:909–23.
60. Kumar S, Kumar R, Goel V, Bhattacharyya S, Issakhov A. Exergetic performance estimation for roughened triangular duct used in solar air heaters. *J Therm Anal Calorim.* 2021;145:1661–72.
61. Velmurugan V, Kalaivanan R. Energy and exergy analysis of multi-pass flat plate solar air heater- an analytical approach. *Int J Green Energy.* 2015;12:810–20.
62. Kumar A, Kumar R, Maithani R, Chauhan R, Kumar S, Nadda R. An experimental study of heat transfer enhancement in an air channel with broken multi type V-baffles. *Heat Mass Trans.* 2017;53:3593–612.
63. Altfeld K, Leiner W, Fiebig M. Second law optimization of flat-plate solar air heaters. *Sol Energy.* 1988;41:127–32.
64. Bhushan B, Singh R. Nusselt number and friction factor correlations for solar air heater duct having artificially roughened absorber plate. *Sol Energy.* 2011;85:1109–18.

Publisher's Note Springer Nature remains neutral with regard to jurisdictional claims in published maps and institutional affiliations.